Spatio-temporal alterations in functional connectivity and white matter microstructure resulting from glucose hypometabolism in a rat model of sporadic Alzheimer's disease

Catarina Tristão Pereira[1,2,†], Yujian Diao[3,†], Carole Poitry-Yamate[1], Ting Yin[1], Analina R da Silva[1], Rolf Gruetter[1,3] and Ileana O Jelescu[1,*]

[1]Centre d'Imagerie Biomédicale, EPFL, Lausanne, Switzerland. [2]Faculdade de Ciências da Universidade de Lisboa, Lisbon, Portugal. [3]Laboratoire d'Imagerie Fonctionnelle et Métabolique, EPFL, Lausanne, Switzerland.

†: These authors contributed equally to the work

Abstract

Impaired brain glucose metabolism has been singled out as an important contributor and possibly main trigger to the development of Alzheimer's disease. Intracerebroventricular injections of streptozotocin (icv-STZ) precisely cause brain glucose hypometabolism without systemic diabetes and are a valuable tool for evaluating ensuing neurodegeneration. Here, a first-time comprehensive longitudinal study of brain glucose metabolism, functional connectivity and white matter microstructure was performed in icv-STZ rats using FDG-PET, resting-state fMRI and diffusion MRI, respectively. STZ rats displayed altered functional connectivity and white matter degeneration in brain regions typically involved in AD, in a temporal pattern of acute injury, transient recovery and chronic degeneration, which did not match the temporal pattern of glucose hypometabolism. This finding supports the hypothesis that a compensatory mechanism, possibly recruiting ketone bodies, can restore normal brain structure and function up to a certain level of pathological severity. This study further highlights the dynamics of how brain insulin resistance affects structure and function and identifies potent MRI-derived biomarkers to track neurodegeneration in human AD and diabetic populations.

Keywords: Alzheimer's disease, streptozotocin, MRI-derived biomarkers, brain glucose metabolism, functional connectivity, microstructure

[*] Address all correspondence to: Dr. Ileana Jelescu, ileana.jelescu@epfl.ch

1. Introduction

Alzheimer's disease (AD) is the most common form of dementia and its incidence outburst already constitutes an economic and social burden. Clinically, AD is manifested by progressive memory loss and gradual decline in cognitive function, often culminating in premature death. However, pathological brain changes in AD begin to develop decades before the first symptoms (Sperling et al., 2011). The characterization of the temporal progression of these changes promises to provide an understanding of disease mechanisms, an effective disease staging and a window for therapeutic intervention.

In that regard, many studies have proposed the order in which relevant biomarkers occur in the progression of disease (Jack et al., 2013; Sperling et al., 2011). The pathological cascade of AD is characterized by initial deposition of amyloid-β (Aβ) plaques in the extracellular space and intracellular neurofibrillary tangles of hyperphosphorylated tau (NFTs) (Dickerson, 2013; Shaw et al., 2009; Wang et al., 2013). In addition, neurodegeneration manifests as reduced brain glucose metabolism (Edison et al., 2007), impaired synaptic activity (Shankar and Walsh, 2009) and neuronal loss (Attwell and Laughlin, 2001; Zarow et al., 2005). Gross cerebral atrophy (Gispert et al., 2015) and white matter degeneration (Chang et al., 2015; Choo et al., 2010; Dong et al., 2020; Jelescu et al., 2018) have been considered relevant biomarkers as well, along with reduced functional connectivity (Binnewijzend et al., 2012; Franzmeier et al., 2019). Nevertheless, the spatio-temporal relationship between AD hallmarks remains unclear.

Meanwhile, hypometabolism of glucose in the brain is taking the center stage as a key player in the onset of AD (Kuehn, 2020), while the amyloid cascade hypothesis is being questioned (Kametani and Hasegawa, 2018). Impaired brain insulin function has been reported to trigger AD pathology (Correia et al., 2011; Hölscher, 2019), while less robust glycolysis has been shown in animals at increased risk for developing dementia (Wu et al., 2018). Moreover, metabolic decline has been linked with impaired glucose transport and neuroinflammation (An et al., 2018; Balducci and Forloni, 2018). As it becomes well-established that diabetes makes the brain more susceptible to the aging process (Gudala et al., 2013), AD pathology has been suggested to be a brain-specific type-III diabetes (de la Monte and Wands, 2008).

Animal models allow studying each of the contributors to the cascade individually and obtaining comprehensive longitudinal data across their lifespan, which is particularly important for disentangling direct effects of contributors and their interactions. Much effort has been put into the development and studies of transgenic mouse models of amyloidosis and tauopathy, which revealed for instance that – in mice – mutations causing amyloidosis alone do not produce NFTs, and tauopathy alone results in a fronto-temporal dementia pattern rather than AD (Buxbaum, 2009). The validity of transgenic animals is also limited in that they are not representative of the sporadic form of the disease, which is the predominant one in humans (King, 2018).

With the importance of brain glucose metabolism in AD being increasingly recognized, animal models of brain insulin resistance have been developed by an intracerebroventricular (icv) injection of streptozotocin (STZ). Intravenous injection of STZ is a very well-established model for type I diabetes (Ganda et al., 1976; Junod et al., 1969). Even though its mechanism is not fully elucidated, when delivered exclusively to the brain via the ventricles, this diabetogenic substance is thought to disrupt the brain insulin receptor system, thereby reducing the glycolytic metabolism in the hippocampus and parieto-temporal cortex, but without causing systemic diabetes (Nitsch and Hoyer, 1991; Plaschke et al., 2010).

Accordingly, icv-STZ rats and monkeys have been shown to develop features typical of AD including memory impairment, NFT changes and extracellular accumulation of Aβ in the neocortex and hippocampus, thinning of the parietal cortex and corpus callosum (Knezovic et al., 2015), neuronal loss, astrocytosis and microgliosis in the corpus callosum and septum (Kraska et al., 2012), axonal damage and demyelination in the hippocampus and fornix (Shoham et al., 2003) and decreased glucose uptake (Heo et al., 2011). Along with disruption of the brain glucose metabolism, STZ induces oxidative stress by impairment of insulin signaling (Lester-Coll et al., 2006; Shoham et al., 2003). The icv-STZ model has clearly demonstrated its potential to reproduce sporadic AD by the resemblance with the behavioral, neurochemical and structural changes found in the human AD brain. However, beyond anatomical data, this animal model has never been assessed with MRI, which could potentially offer significant insight into neurodegenerative processes.

We hypothesize that MRI-derived metrics of microstructure and functional connectivity in icv-STZ rats should show the same bi-phasic pattern as reported in human AD (Dickerson et al., 2005; Dong et al., 2020; Montal et al., 2018), with early inflammation followed by remission due to compensatory mechanisms and chronic neurodegeneration. Furthermore, in icv-STZ rats we could determine how these changes relate to glucose hypometabolism.

Here we therefore performed a longitudinal study in the icv-STZ rat model to quantitatively characterize alterations in functional connectivity and in white matter microstructure using resting-state functional (rs-fMRI) and diffusion MRI, respectively, as well as changes in brain glucose uptake captured by 18FDG-PET. This study highlights the dynamics of how insulin resistance affects brain structure and function in a spatio-temporal pattern and serves the dual purpose of outlining pathological trajectories relevant for clinical studies and validating potent MRI-derived biomarkers to track neurodegeneration in human AD and diabetes populations.

2. Methods

2.1. Animals

Animal experiments were approved by the Service for Veterinary Affairs of the canton of Vaud. Male Wistar rats (Charles River, l'Arbresle, France) weighing 225-247 g at baseline were assessed at four timepoints after the icv injection: PET and MRI data were collected at 2, 6, 13 and 21 weeks following surgery (**Fig. 1**) and rats were sacrificed by perfusion fixation after the last assessment.

2.2. Intracerebroventricular injection

Rats were anesthetized using isoflurane (4% for induction and 2% for maintenance) and positioned in a stereotaxic frame (KopfModel900). The head was shaved and the skull was exposed with a midline incision. Two holes were burred into the skull, giving access to the two lateral ventricles at stereotaxic coordinates: ±1.4 mm lateral, 0.9 posterior and 3.5 mm deep relative to the bregma. A single bilateral icv injection (2 µL in each ventricle) of either 3 mg/kg STZ dissolved in citrate buffer (STZ group, n = 9), or citrate buffer solution (0.05 M, pH = 4.5) (control group, CTL, n = 8) was performed at a rate of 5 uL/h using Hamilton syringes, a double-syringe pump (TSE System) and catheters with 30G needles. At the end of the perfusion, the catheters were removed and the skin was sutured with silk sutures 3/0. Rats were allowed to recover for two weeks before the first scanning session.

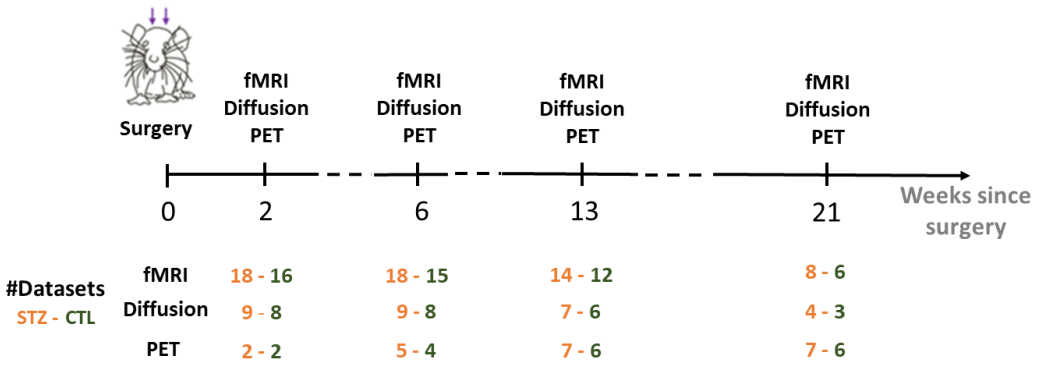

Figure 1: Experimental timeline. PET and MRI data were collected at 2, 6, 13 and 21 weeks after icv-STZ injection. Two fMRI runs were acquired for each MRI session, which explains the larger number of datasets. All animals could not be scanned at the 21-week timepoint due to a major MRI hardware upgrade at our center before the study was completed.

2.3. FDG-PET data acquisition

Animal preparation

Rats housed with free access to food and water were initially anesthetized using isoflurane (2% for induction) in an oxygen/air mixture of 30%/70% during tail vein cannulation for tracer delivery, and then isoflurane (1-2%) in 100% oxygen via a nose-cone once the animal was transferred and prone positioned on a temperature regulated PET scanner bed. Within the first minute of PET acquisition, a bolus of roughly 50 MBq 18F-FDG (Advanced Accelerator Applications, Geneva, Switzerland) was manually injected through the tail vein and followed by a saline chase. Throughout the experiment, breathing rate and body temperature were monitored using a respiration pillow and a rectal thermometer, respectively. Body temperature was maintained around (37±0.5) ºC. Pre- and post-scan glycemia were determined from blood at the tail vein cannulation site using a Bayer glucose meter.

PET acquisition

All PET experiments were performed on an avalanche photodiode-based LabPET-4 small-animal scanner (Gamma Medica-Ideas Inc.) as described in (Lanz et al., 2014). Briefly, data were collected in list-mode and images between 30 and 50 minutes after injection were reconstructed using the maximum likelihood expectation maximization iterative reconstruction algorithm with a circular field of view (FOV) of 80 mm. The reconstructed voxel size was 0.25 x 0.25 x 1.18 mm. The Standardized Uptake Value (SUV) was normalized to generate steady-state images.

2.4. MRI data acquisition

Animal preparation

Animals were initially anesthetized using isoflurane (4% for induction and 1-2% for maintenance in an oxygen/air mixture of 30%/70%) and positioned in a homemade MRI cradle equipped with a fixation system (bite bar and ear bar). A catheter was inserted subcutaneously on the back of the animal for later medetomidine delivery. One hour before starting the rs-fMRI acquisition, anesthesia was switched from isoflurane to medetomidine (Dorbene, Graeub, Switzerland), which preserves neural activity and vascular response better than isoflurane (Pawela et al., 2009; Weber et al., 2006), with an initial bolus of 0.1 mg/kg followed by a continuous perfusion of 0.1 mg/kg/h (Reynaud et al., 2019).

Throughout the experiment, the breathing rate and the body temperature were monitored similarly to the PET acquisition. At the end of the scanning session, animals were woken up with an intramuscular injection of atipamezole (Alzane, Graeub, Switzerland) at 0.5 mg/kg.

MRI acquisition

All MRI experiments were performed on a 14 T Varian system (Abingdon, UK) equipped with 400 mT/m gradients. An in-house built quadrature surface coil was used for transmission and reception.

Structural T_2-weighted images were collected using a fast spin-echo sequence with the following parameters: TE/TR = 10.17/3000 ms, echo train length: 4, matrix size = 128 x 128, FOV = 19.2 x 19.2 mm^2, voxel size = 0.15 x 0.15 mm^2, 30 coronal 0.5-mm slices, scan time = 10 minutes.

Diffusion-weighted data were acquired using a semi-adiabatic pulsed-gradient spin-echo (PGSE) segmented EPI sequence (van de Looij et al., 2011), with the following protocol: 4 b = 0 images and 3 shells at b = 0.8 / 1.3 / 2.0 ms/μm^2, with 12, 16 and 30 directions, respectively; δ/Δ = 4/27 ms; TE/TR = 48/2500 ms; 4 shots; matrix size = 128 x 64, FOV = 23 x 17 mm^2, voxel size = 0.18 x 0.27 mm^2, 9 coronal 1-mm slices, 4 repetitions, scan time = 1 hour.

Rs-fMRI data were acquired using a two-shot gradient-echo EPI sequence as follows: TE/TR = 10/800 ms, TR_{vol} = 1.6 s, matrix size = 64 x 64, FOV = 23 x 23 mm^2, voxel size = 0.36 x 0.36 mm^2 and 8 coronal 1.12-mm slices, 370 repetitions, scan time = 10 minutes. Two fMRI runs were acquired in each MRI session.

2.5. Image processing

2.5.1. FDG uptake

FDG-PET steady-state SUV maps were registered to their corresponding T_2-weighted anatomical MR images with cross-correlation using ANTs (Avants et al., 2011, 2008), which was in turn registered to the Waxholm Space Atlas of the rat brain (https://www.nitrc.org/projects/whs-sd-atlas) using linear and non-linear registration (Avants et al., 2011) and 26 regions of interest (ROI) were automatically segmented. SUV images were normalized by the mean SUV over the brain (SUVr – relative SUV) to correct for inter-rat experimental variability (Heo et al., 2011).

2.5.2. Resting-state functional connectivity

The rs-fMRI pre-processing pipeline is described in detail in (Diao et al., 2020). Briefly, images were skull-stripped, denoised (in the sense of thermal noise reduction) using a novel Marchenko Pastur PCA approach (Ades-Aron et al., 2018; Does et al., 2019; Veraart et al., 2016), corrected for EPI-related distortions using FSL's topup (Smith et al., 2004), slice-timing corrected and spatially smoothed with a 0.36 x 0.36 x 1 mm^3 full width half maximum (FWHM) kernel (Friston et al., 2007). Independent component analysis (ICA) was run on the fMRI timecourses using FSL's MELODIC (Beckmann and Smith, 2004), with a high-pass filter (f > 0.01 Hz) and 40 components. All ICA decompositions were run through a dedicated rat FMRIB's ICA-based Xnoiseifier (FIX) classifier (Diao et al., 2020), as previously described for humans and mice (Griffanti et al., 2017; Zerbi et al., 2015) and artefactual independent components attributable to physiological noise were automatically removed from the signal. Corrected fMRI images were registered to the anatomical image and then to the Waxholm Space Atlas using linear and non-linear registration in FSL (Jenkinson et al., 2002) and 28 atlas-defined ROIs (14 per hemisphere) were automatically segmented. Lastly, mean fMRI timecourses were extracted for each ROI based on "FIX-cleaned" data and individual ROI-to-ROI functional connectivity matrices were computed by calculating partial correlation between timecourses covarying for the global signal.

2.5.3. Diffusion MRI and white matter microstructure

Pre-processing diffusion data included denoising using random matrix theory (Veraart et al., 2016) followed by Gibbs-ringing correction (Kellner et al., 2016) and correction for EPI-related distortions, eddy currents and motion using FSL's eddy (Andersson and Sotiropoulos, 2016). The diffusion and kurtosis tensors were estimated using a weighted linear least squares algorithm (Jensen et al., 2005; Veraart et al., 2013) and typical DTI and DKI-derived metrics were calculated: fractional anisotropy (FA), mean/axial/radial diffusivity (MD/AxD/RD) and mean/axial/radial kurtosis (MK/AK/RK). To overcome the lack of specificity inherent to empirical representations such as DTI and DKI, the biophysical White Matter Tract Integrity (WMTI) model was computed in white matter voxels using a Watson distribution of axon orientations (Fieremans et al., 2011; Jespersen et al., 2018). The following microstructure parameters were extracted from the model: the intra-axonal water fraction f, the parallel intra-axonal diffusivity D_a, the parallel $D_{e,\parallel}$ and perpendicular $D_{e,\perp}$ extra-axonal diffusivity and the orientation distribution c_2 (**Fig. 2**) . This model has two mathematical solutions (Fieremans et al., 2011; Jelescu et al., 2016; Novikov et al., 2018), of which the $D_a > D_{e,\parallel}$ solution was retained, according to recent evidence (Dhital et al., 2019; Jespersen et al., 2018; Kunz et al., 2018; Veraart et al., 2018). FA maps were registered to a FA template in the Waxholm Space using linear and non-linear registration in FSL (Jenkinson et al., 2002) and the corpus callosum, cingulum and fimbria of the hippocampus were automatically segmented. This approach enabled a more accurate segmentation of the white matter tracts, that otherwise tend to be misaligned due to enlargement of ventricles in STZ rats. Diffusion metrics were averaged over white matter ROIs.

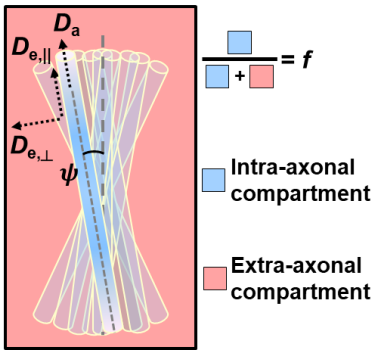

Figure 2: Schematics of the WMTI-Watson biophysical model *(Jelescu and Budde, 2017; Jespersen et al., 2018)*. The diffusion signal is described in terms of two non-exchangeable compartments, the intra and extra-axonal spaces. Here, the axons are modelled as long narrow cylinders that reproduce a highly anisotropic medium. The intra-axonal space is described by a volume fraction of water molecules f and the parallel intra-axonal diffusivity D_a. The perpendicular intra-axonal diffusivity is negligible at the relevant diffusion times, such that axons are considered to have radius equal to zero. The bundle of axons is embedded in the extra-axonal space that yields the parallel $D_{e,\parallel}$ and the perpendicular extra-axonal diffusivities $D_{e,\perp}$. The axons' orientations are modeled by a Watson distribution, which is characterized by $\langle(\cos\psi)^2\rangle \equiv c_2$.

2.5.4. Statistical analysis

Rats' weight was compared between STZ and CTL groups at each timepoint using two-tailed Mann-Whitney U-test, at significance level of $\alpha = 0.05$. In this analysis, we included 9/8 STZ/CTL at 2 weeks after injection, 9/8 STZ/CTL at 6 weeks, 9/8 STZ/CTL at 13 weeks and 5/5 STZ/CTL at 21 weeks.

FDG uptake: Regional differences in SUVr between STZ and CTL groups were evaluated at each timepoint using one-tailed Mann-Whitney *U*-test (STZ>CTL), at significance level of α = 0.05. Here, we included 2/2 STZ/CTL rats at 2 weeks after injection, 5/4 STZ/CTL at 6 weeks, 7/6 STZ/CTL at 13 weeks and 7/6 STZ/CTL at 21 weeks (**Fig. 1**).

Resting-state functional connectivity: The significance of group differences was tested using non-parametric permutation tests (N=5000) with the Network-Based Statistics (NBS) Toolbox, with statistical significance retained at $p = 0.05$ after family-wise error rate (FWER) correction. Here, we included 18/16 STZ/CTL fMRI runs at 2 weeks after injection, 18/15 STZ/CTL at 6 weeks, 14/12 STZ/CTL at 13 weeks and 8/6 STZ/CTL at 21 weeks (**Fig. 1**).

White matter microstructure: Average diffusion-derived metrics in each white matter ROI were compared between STZ and CTL groups at each timepoint using two-tailed Mann-Whitney *U*-test, at a α = 0.05 significance. Longitudinal changes within each group were assessed by one-way ANOVA and Tukey-Cramer correction, at a α = 0.05 significance. Here, 9/8 STZ/CTL rats were included at 2 weeks after injection, 9/8 STZ/CTL at 6 weeks, 7/6 STZ/CTL at 13 weeks and 4/3 STZ/CTL at 21 weeks (**Fig 1**).

3. Results

3.1. Weight

The weight of all animals was measured before the icv-STZ injection (baseline) and at all timepoints before each MRI scanning session. There was no difference between groups at baseline and at 21 weeks, but STZ rats had a significantly lower weight than CTL rats at 2, 6 and 13 weeks after the injection (**Fig. 3**).

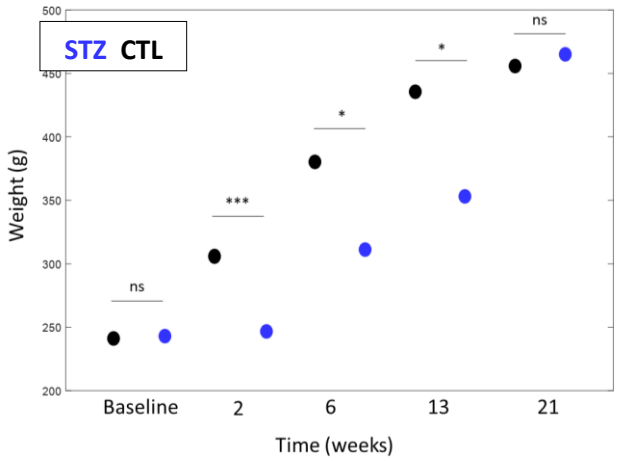

Figure 3: Group differences in rats' weight measured before icv-STZ injection (baseline) and at all timepoints. ns: non-significant, *: $p < 0.05$, ***: $p < 0.001$ using the Mann-Whitney *U*-test.

3.2. FDG uptake

SUVr was reduced in STZ rats compared to CTL rats, with different spatial patterns over time (**Fig. 4**). At 2 weeks after injection, there were no differences between the STZ and the CTL groups but the sample size was also very limited at that timepoint (2 animals per group). The most pronounced differences were found at 6 weeks after injection, involving several regions typically affected in AD. Lower SUVr was found in the anterior cingulate cortex (ACC) more significantly, but also in the retrosplenial cortex (RSC), the posterior parietal cortex (PPC), the motor, somatosensory, auditory and visual cortices. The medial temporal lobe (MTL) and the hippocampus (including subiculum) displayed a trend for lower

SUVr with $p < 0.1$. Later, STZ rats showed less significant group differences throughout the brain, with the MTL being affected at 13 weeks and 21 weeks after injection. At 21 weeks, the ACC, RSC and PPC show a trend for lower SUVr with $p < 0.1$.

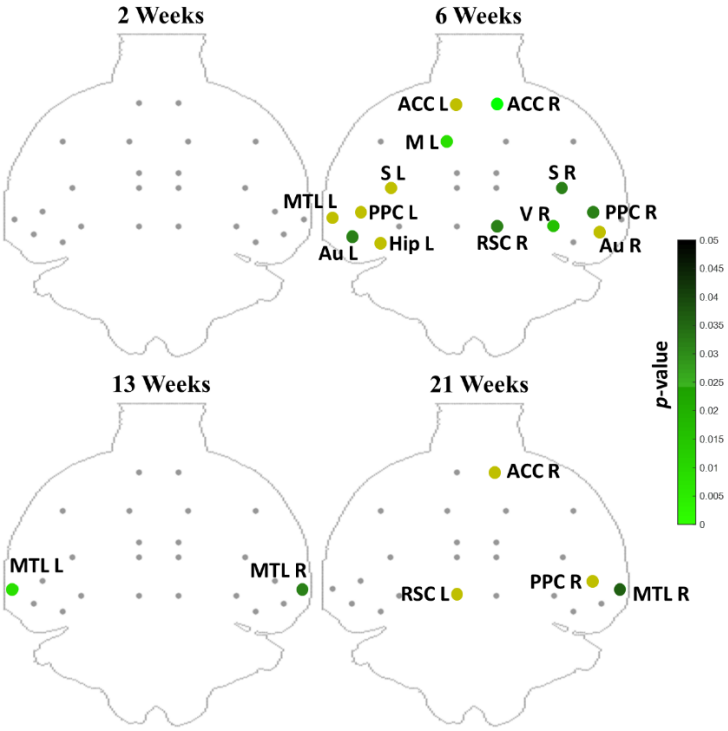

Figure 4: Group differences in SUVr at each timepoint. Green: ROIs with significantly lower SUV ($p < 0.05$ using one-tailed Mann-Whitney *U*-test, STZ < CTL). Dark yellow: Trend of lower SUV ($p < 0.1$). Correction for multiple comparisons was not applied given the small number of animals per group. ACC: anterior cingulate cortex; RSC: retrosplenial cortex; PPC: posterior parietal cortex; MTL: medial temporal lobe; Hip: hippocampus; Au: auditory; V: visual; S: somatosensory; M: motor; L/R: left/right.

3.3. Resting-state functional connectivity

Significant group differences in functional connectivity were found at 2, 13 and 21 weeks after injection (**Fig. 5A**). In the **Fig. 5B** graph networks highlight the group differences in nodal connections. At 2 weeks after injection, connections of the ACC to the PPC, hippocampus, subiculum and somatosensory, auditory and visual cortices were primarily affected in the STZ group, particularly in the right hemisphere. At 13 weeks, bilateral changes in connectivity involving ACC, PPC but also striatum as well as motor and somatosensory cortices were found. Altered functional connectivity evolved towards the posterior and temporal brain regions at 21 weeks, where connectivity differences were most pronounced. Here, strong inter-hemispheric alterations were found in all previously mentioned areas as well as MTL and RSC. Remarkably, STZ rats exhibited a non-monotonic trend in functional connectivity alterations, with temporary recovery at 6 weeks after injection.

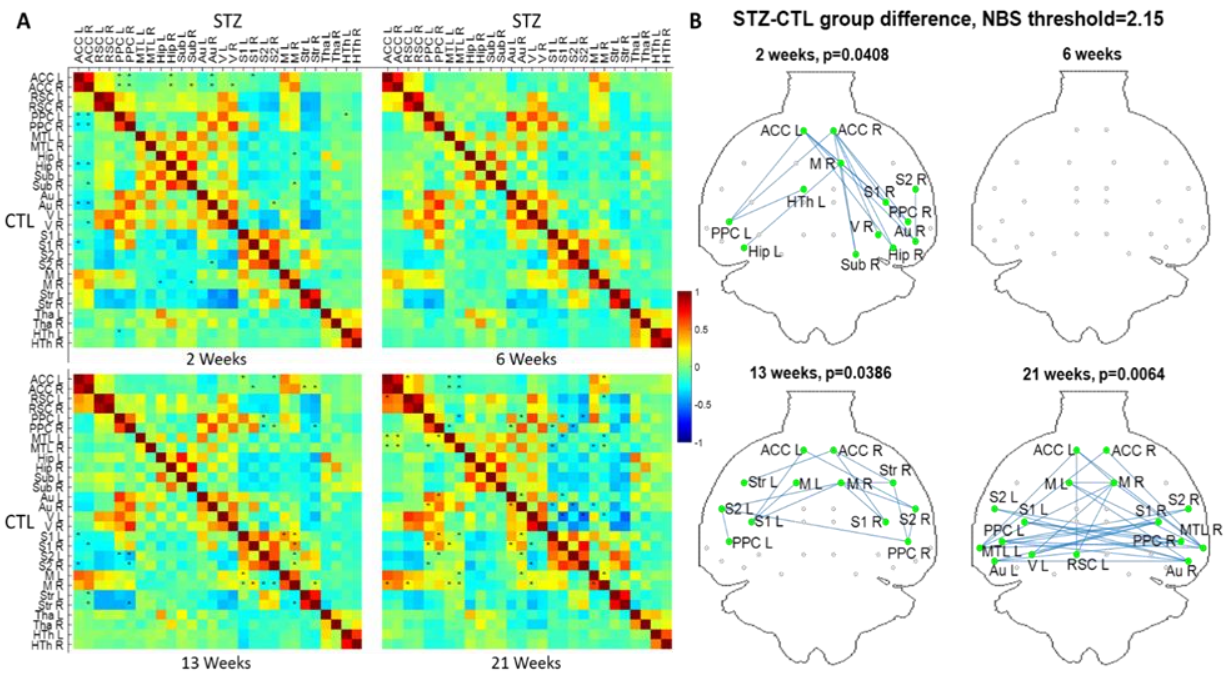

Figure 5: **A)** Hybrid average functional connectivity matrices at each timepoint (top-right half: STZ, bottom-left half: CTL). *: $p < 0.05$ (FWER corrected) at a threshold of 2.15. **B)** Graph networks at each timepoint. Blue edges and green nodes indicate connections with significant difference. The p-value for each network was given after FWER correction. ACC: anterior cingulate cortex; RSC: retrosplenial cortex; PPC: posterior parietal cortex; MTL: medial temporal lobe; Hip: hippocampus; Sub: subiculum; Au: auditory; V: visual; S1/S2: primary/secondary somatosensory; M: motor; Str: striatum; Tha: thalamus; HTh: hypothalamus; L/R: left/right.

3.4. White matter microstructure

Tensor-derived metrics provided differences between groups very marked in the corpus callosum and fimbria of the hippocampus and more mildly in the cingulum (**Fig. 6**). Compared to controls, STZ rats displayed lower FA in the corpus callosum at 2, 6 and 13 weeks after injection, in the fimbria at 2 and 13 weeks and in the cingulum at 13 weeks only. DKI-derived metrics only captured group differences at 13 weeks after injection, with MK being reduced in the STZ group in all ROIs. STZ rats also displayed lower AK and RK at 13 weeks in the corpus callosum and the fimbria and lower RK in the cingulum (not shown). In the CTL group, the AK increased significantly over time. It is noteworthy that the fimbria of the hippocampus was the white matter tract with the largest differences between STZ and CTL rats.

Biophysical modeling provided a more complete information about white matter degeneration (**Fig. 7**). In the corpus callosum, both axonal water fraction f and intra-axonal diffusivity D_a were reduced in the STZ group at 2 weeks and 13 weeks. In the fimbria, f was lower in the STZ group at all timepoints, being more accentuated at 13 weeks, when D_a was also lower. In the cingulum, reduced f was found at 13 weeks. Other model metrics did not show significant changes between groups or with time. Similarly to functional connectivity, white matter microstructure displayed a non-monotonic trend with partial recovery at 6 weeks.

No differences were found at 21 weeks between groups, which could be due to both a reduced cohort size (the last timepoint could not be acquired for a subset of animals due to substantial hardware changes at our center before the study was completed) and aging of control animals.

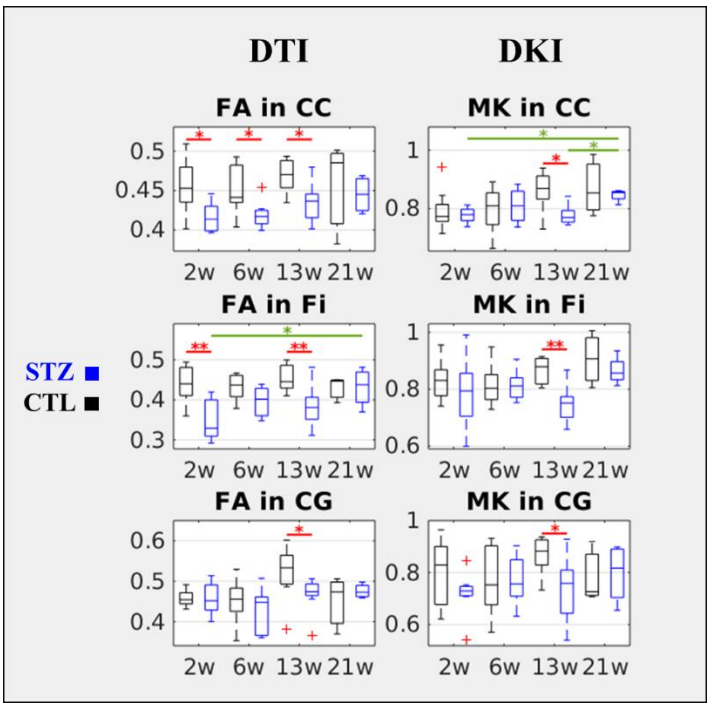

Figure 6: DTI and DKI estimates in the 3 white matter ROIs (top row: corpus callosum (CC), middle row: fimbria of the hippocampus (FI) and bottom row: cingulum (CG)). FA: Fractional Anisotropy, MK: Mean Kurtosis. Sample size is likely too small at 21 weeks. *: $p < 0.05$, **: $p < 0.01$ using the two-tailed Mann-Whitney *U*-test.

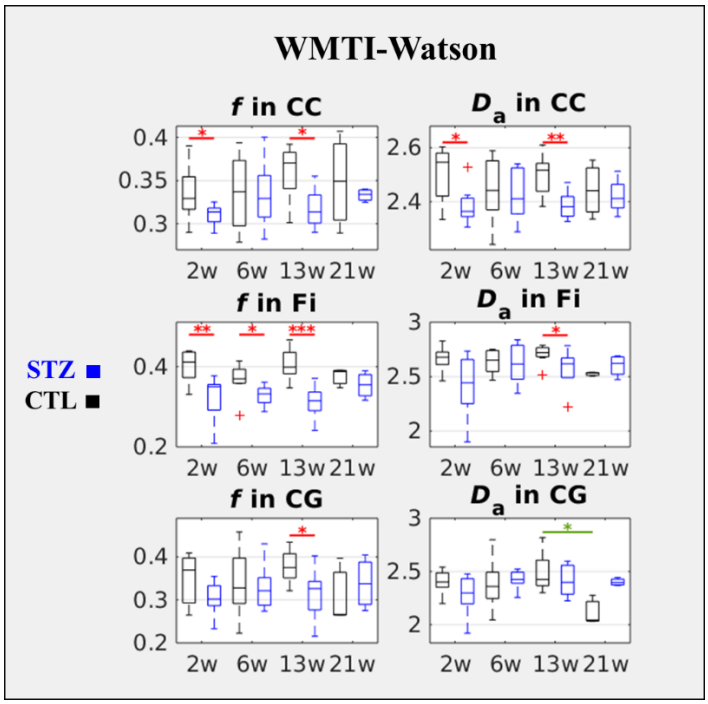

Figure 7: WMTI-Watson model estimates in the 3 white matter ROIs (top row: corpus callosum (CC), middle row: fimbria of the hippocampus (FI) and bottom row: cingulum (CG)). f: intra-axonal water volume fraction, D_a: intra-axonal parallel diffusivity. Sample size is likely too small at 21 weeks. *: $p < 0.05$, **: $p < 0.01$, ***: $p < 0.001$ using one-way ANOVA and Tukey-Cramer correction.

4. Discussion

The icv-STZ animal model has reportedly shown alterations typical of AD, reinforcing the idea that neurodegeneration might be primarily induced by an insulin resistance in the brain. Its effects on the pathological cascade are however not fully understood, and the present study attempts to characterize it by means of MRI-derived biomarkers for the first time. In this longitudinal assessment, FDG uptake, resting-state functional connectivity and white matter microstructure results agree in terms of spatio-temporal variations and are consistent with previous findings of cognitive decline, histological and immunochemistry studies.

Alterations in functional connectivity displayed a varying spatio-temporal pattern in STZ animals, with temporary recovery at 6 weeks after injection. The main hub at 2 and 13 weeks after injection was the ACC with altered connections to regions typically involved in AD. Early differences affected mostly the right hemisphere while later differences evolved towards the posterior and temporal brain regions with strong inter-hemispheric alterations.

White matter degeneration was manifested in reduced anisotropy and kurtosis in the STZ group in the corpus callosum and fimbria at 2 and 13 weeks after injection. The specific characterization of the damage was further improved by white matter modeling. Reduced axonal diffusivity D_a and axonal fraction f at 2 weeks and 13 weeks after injection are indicative of axonal injury and loss in the corpus callosum and the fimbria. The effect on the cingulum was less dramatic, where reduced axonal fraction f was found at 13 weeks after injection. The absence of changes in the other model parameters contributes to a specific picture of white matter microstructure alterations, with most damage being attributed to the intra-axonal space and resulting in axonal degeneration, which is consistent with intra-cellular toxic action of STZ (Knezovic et al., 2015; Lester-Coll et al., 2006).

Overall, microstructural alterations agreed with changes in functional connectivity, with marked acute and chronic changes at 2 and 13 weeks, respectively, and fewer differences at 6 weeks. The corpus callosum and the fimbria microstructure appeared to be affected simultaneously to the connectivity of the hippocampus, subiculum and PPC to the ACC in a partially cross-hemispheric fashion, while MTL and RSC only displayed altered functional connectivity to the ACC at 21 weeks, following changes in cingulum microstructure detected at 13 weeks.

These findings are consistent with reported neuronal loss in the septum and corpus callosum at 4 weeks after icv-injection (Kraska et al., 2012) and with thinning of the parietal cortex and the corpus callosum (Knezovic et al., 2015). The latter study also found early neurofibrillary changes at 12 weeks after injection followed by presence of diffuse Aβ plaques in the hippocampus. Furthermore, demyelination in the hippocampus in association with microglia activation has been reported at 6 weeks (Shoham et al., 2003), even though in our study the WMTI-Watson model did not provide evidence for neuroinflammation (in the form of reduced extra-axonal diffusivities) in any of the white matter tracts over the course of our experimental timeline.

FDG-PET data showed reduced glucose uptake in icv-STZ rats in regions typically involved in AD, and are consistent with reported changes in FDG uptake in the MTL of icv-STZ monkeys as early as 2 weeks after injection (Heo et al., 2011). The most pronounced uptake differences in our study were found at 6 weeks, although glucose hypometabolism as early as 2 weeks cannot be excluded. The absence of SUVr group differences at that timepoint is likely due to very limited PET cohort size (2 animals per group, Fig. 1). STZ rats were on average 70 g lighter than CTL rats starting 2 weeks after the STZ injection (Fig. 3), which supports the assumption of impaired brain glucose metabolism as early as 2 weeks and the use of alternative energy sources such as stored body fat, which when burnt results in a buildup of ketones. Ketone

bodies have been referred to as a “brain reserve” that can be mobilized to compensate for an inability to efficiently utilize glucose (Gano et al., 2014; Wu et al., 2018). Remarkably, 6 weeks corresponded to the timepoint of “temporary recovery” in terms of white matter microstructure and functional connectivity metrics. This observation follows the axiom that metabolism underlies structure and function, and indicates that past the acute phase, the brain may switch to other forms of energy, such as ketone bodies as a means to maintain energy homeostasis and restore normal brain function (Yang et al., 2019). Interestingly, the same regions with reduced glucose metabolism at 6 weeks after injection also showed altered functional connectivity later at 13 weeks, supporting the manifestation of a chronic phase of disease. Here, our data suggests that neurodegeneration resumes as pathological mechanisms approach a critical stage and can no longer be compensated for.

The succession of acute change, remission and chronic degeneration phases has also been reported in a nine-month follow-up of memory performance in icv-STZ rats, measured using a passive avoidance test (Knezovic et al., 2015). In this cognitive study however, the examination timepoints were different from ours and the acute phase was found at 1 month after injection, the recovery period between 3 and 6 months and chronic decrease of latency time from 6 months on. The progression of the MRI-derived biomarkers of neurodegeneration used in this study was qualitatively overlaid with that of memory performance from (Knezovic et al., 2015) for comparison (**Fig. 8**). The trends in white matter microstructure and functional connectivity clearly provide earlier evidence of brain changes in the icv-STZ model than behavioral observations, as MRI-derived biomarkers are expected to be more sensitive to mechanisms occurring in the preclinical stage of the pathological cascade. Such neuroimaging trends could potentially predict the following symptomatic stage of the disease that includes cognitive deficits.

Non-monotonic and biphasic trajectories of brain alterations have also been reported in several human studies of AD and mild cognitive impairment, and involve a variety of biomarkers from cortical volumes, cerebral perfusion, gray and white matter microstructure, and hippocampal activity (Dickerson et al., 2005; Dong et al., 2020; Fortea et al., 2014, 2011; Montal et al., 2018; Pegueroles et al., 2017; Sierra-Marcos, 2017).

The quantification of functional connectivity and white matter degeneration has provided insightful information about spatial and temporal AD-like changes induced by brain glucose hypometabolism. The present study contributes to the growing hypothesis that brain insulin resistance is a key player in the onset of Alzheimer’s disease and the icv-STZ rat model offers great potential for the investigation of neurodegeneration in the context of AD and diabetes. For a complete picture of the pathological cascade in this animal model, a future longitudinal study should include MRI, PET, behavior and cross-sectional histology all at once.

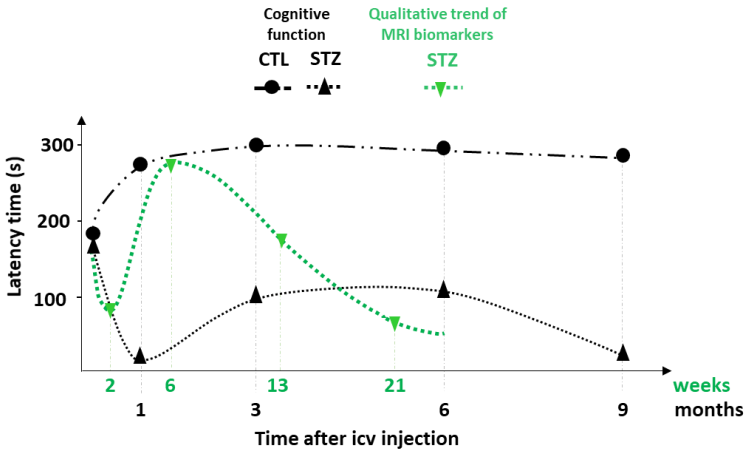

Figure 8: Progression of MRI biomarkers in comparison with memory performance in the icv-STZ rat model. Figure adapted from *(Knezovic et al., 2015)*. Black: Latency time measured in the passive avoidance test reported in *(Knezovic et al., 2015)* as a function of time in months. Green: Qualitative trend of the MRI biomarkers reported in the present study as function of time in weeks.

5. Conclusion

In this work, we used the icv-STZ rat model to characterize longitudinal alterations in brain functional connectivity and white matter microstructure resulting from impaired brain glucose metabolism. Icv-STZ animals displayed early altered connectivity of the ACC and later of the temporal and posterior brain regions. Moreover, white matter degeneration was manifested as axonal injury and loss, mainly affecting the corpus callosum and the fimbria. MRI-derived biomarkers presented changes with a similar spatio-temporal pattern and in agreement with existing literature. They followed a sequence of early acute injury followed by transient recovery and late chronic degeneration. In parallel, brain glucose hypometabolism was likely established from the start. The transient recovery in brain structure and function is interpreted as the recruitment of alternative forms of energy such as ketone bodies to make up for impaired glucose metabolism, until pathological mechanisms are no longer reversible. Our study supports the hypothesis of impaired insulin/glucose metabolism as a key player in the onset of AD and the relevance of the icv-STZ animal models for pre-clinical AD research.

Acknowledgments

The authors thank Mario Lepore and Stefan Mitrea for assistance with animal setup and monitoring. This work was supported by the Centre d'Imagerie BioMédicale (CIBM) of the University of Lausanne (UNIL), the Swiss Federal Institute of Technology of Lausanne (EPFL), the University of Geneva (UniGe), the Centre Hospitalier Universitaire Vaudois (CHUV), the Hôpitaux Universitaires de Genève (HUG) and the Leenaards and the Jeantet Foundations. C.T.P. acknowledges the support of the Swiss-European Mobility Plan (Movetia).

References

Ades-Aron, B., Veraart, J., Kochunov, P., McGuire, S., Sherman, P., Kellner, E., Novikov, D.S., Fieremans, E., 2018. Evaluation of the accuracy and precision of the diffusion parameter EStImation with Gibbs and NoisE removal pipeline. NeuroImage 183, 532–543. https://doi.org/10.1016/j.neuroimage.2018.07.066

An, Y., Varma, V.R., Varma, S., Casanova, R., Dammer, E., Pletnikova, O., Chia, C.W., Egan, J.M., Ferrucci, L., Troncoso, J., Levey, A.I., Lah, J., Seyfried, N.T., Legido-Quigley, C., O'Brien, R., Thambisetty, M., 2018. Evidence for brain glucose dysregulation in Alzheimer's disease. Alzheimers Dement. 14, 318–329. https://doi.org/10.1016/j.jalz.2017.09.011

Andersson, J.L.R., Sotiropoulos, S.N., 2016. An integrated approach to correction for off-resonance effects and subject movement in diffusion MR imaging. NeuroImage 125, 1063–1078. https://doi.org/10.1016/j.neuroimage.2015.10.019

Attwell, D., Laughlin, S.B., 2001. An Energy Budget for Signaling in the Grey Matter of the Brain. J. Cereb. Blood Flow Metab. 21, 1133–1145. https://doi.org/10.1097/00004647-200110000-00001

Avants, B., Epstein, C., Grossman, M., Gee, J., 2008. Symmetric diffeomorphic image registration with cross-correlation: Evaluating automated labeling of elderly and neurodegenerative brain. Med. Image Anal. 12, 26–41. https://doi.org/10.1016/j.media.2007.06.004

Avants, B., Tustison, N., Song, G, Cook, P.A., Klein, A., Gee, J.C., 2011. A reproducible evaluation of ANTs similarity metric performance in brain image registration. NeuroImage 54, 2033–2044. https://doi.org/10.1016/j.neuroimage.2010.09.025

Balducci, C., Forloni, G., 2018. Novel targets in Alzheimer's disease: A special focus on microglia. Pharmacol. Res. 130, 402–413. https://doi.org/10.1016/j.phrs.2018.01.017

Beckmann, C.F., Smith, S.M., 2004. Probabilistic Independent Component Analysis for Functional Magnetic Resonance Imaging. IEEE Trans. Med. Imaging 23, 137–152. https://doi.org/10.1109/TMI.2003.822821

Binnewijzend, M.A.A., Schoonheim, M.M., Sanz-Arigita, E., Wink, A.M., van der Flier, W.M., Tolboom, N., Adriaanse, S.M., Damoiseaux, J.S., Scheltens, P., van Berckel, B.N.M., Barkhof, F., 2012. Resting-state fMRI changes in Alzheimer's disease and mild cognitive impairment. Neurobiol. Aging 33, 2018–2028. https://doi.org/10.1016/j.neurobiolaging.2011.07.003

Buxbaum, J.N., 2009. Animal models of human amyloidoses: Are transgenic mice worth the time and trouble? FEBS Lett. 583, 2663–2673. https://doi.org/10.1016/j.febslet.2009.07.031

Chang, Y.-L., Chen, T.-F., Shih, Y.-C., Chiu, M.-J., Yan, S.-H., Tseng, W.-Y.I., 2015. Regional Cingulum Disruption, Not Gray Matter Atrophy, Detects Cognitive Changes in Amnestic Mild Cognitive Impairment Subtypes. J. Alzheimers Dis. 44, 125–138. https://doi.org/10.3233/JAD-141839

Choo, I.H., Lee, D.Y., Oh, J.S., Lee, J.S., Lee, D.S., Song, I.C., Youn, J.C., Kim, S.G., Kim, K.W., Jhoo, J.H., Woo, J.I., 2010. Posterior cingulate cortex atrophy and regional cingulum disruption in mild cognitive impairment and Alzheimer's disease. Neurobiol. Aging 31, 772–779. https://doi.org/10.1016/j.neurobiolaging.2008.06.015

Correia, S.C., Santos, R.X., Perry, G., Zhu, X., Moreira, P.I., Smith, M.A., 2011. Insulin-resistant brain state: The culprit in sporadic Alzheimer's disease? Ageing Res. Rev. 10, 264–273. https://doi.org/10.1016/j.arr.2011.01.001

de la Monte, S.M., Wands, J.R., 2008. Alzheimer's Disease is Type 3 Diabetes—Evidence Reviewed. J. Diabetes Sci. Technol. 2, 1101–1113. https://doi.org/10.1177/193229680800200619

Dhital, B., Reisert, M., Kellner, E., Kiselev, V.G., 2019. Intra-axonal diffusivity in brain white matter. NeuroImage 189, 543–550. https://doi.org/10.1016/j.neuroimage.2019.01.015

Diao, Y., Yin, T., Gruetter, R., Jelescu, I.O., 2020. An optimized pipeline for functional connectivity analysis in the rat brain. ArXiv200109857 Phys. Q-Bio.

Dickerson, B., 2013. Biomarker-based prediction of progression in MCI: comparison of AD signature and hippocampal volume with spinal fluid amyloid-β and tau. Front. Aging Neurosci. 5. https://doi.org/10.3389/fnagi.2013.00055

Dickerson, B.C., Salat, D.H., Greve, D.N., Chua, E.F., Rand-Giovannetti, E., Rentz, D.M., Bertram, L., Mullin, K., Tanzi, R.E., Blacker, D., Albert, M.S., Sperling, R.A., 2005. Increased hippocampal activation in

mild cognitive impairment compared to normal aging and AD. Neurology 65, 404. https://doi.org/10.1212/01.wnl.0000171450.97464.49

Does, M.D., Olesen, J.L., Harkins, K.D., Serradas-Duarte, T., Gochberg, D.F., Jespersen, S.N., Shemesh, N., 2019. Evaluation of principal component analysis image denoising on multi-exponential MRI relaxometry. Magn. Reson. Med. mrm.27658. https://doi.org/10.1002/mrm.27658

Dong, J.W., Jelescu, I.O., Ades-Aron, B., Novikov, D.S., Friedman, K.P., Osorio, R., Galvin, J.E., Shepherd, T.M., Fieremans, E., 2020. Diffusion MRI biomarkers of white matter microstructure vary nonmonotonically with increasing cerebral amyloid deposition. Neurobiol. Aging.

Edison, P., Archer, H.A., Hinz, R., Hammers, A., Pavese, N., Tai, Y.F., Hotton, G., Cutler, D., Fox, N., Kennedy, A., Rossor, M., Brooks, D.J., 2007. Amyloid, hypometabolism, and cognition in Alzheimer disease: An [11C]PIB and [18F]FDG PET study. Neurology 68, 501–508. https://doi.org/10.1212/01.wnl.0000244749.20056.d4

Fieremans, E., Jensen, J.H., Helpern, J.A., 2011. White matter characterization with diffusional kurtosis imaging. Neuroimage 58, 177–88. https://doi.org/10.1016/j.neuroimage.2011.06.006

Fortea, J., Sala-Llonch, R., Bartrés-Faz, D., Lladó, A., Solé-Padullés, C., Bosch, B., Antonell, A., Olives, J., Sanchez-Valle, R., Molinuevo, J.L., Rami, L., 2011. Cognitively Preserved Subjects with Transitional Cerebrospinal Fluid ß-Amyloid 1-42 Values Have Thicker Cortex in Alzheimer's Disease Vulnerable Areas. Biol. Psychiatry 70, 183–190. https://doi.org/10.1016/j.biopsych.2011.02.017

Fortea, J., Vilaplana, E., Alcolea, D., Carmona-Iragui, M., Sánchez-Saudinos, M.-B., Sala, I., Antón-Aguirre, S., González, S., Medrano, S., Pegueroles, J., Morenas, E., Clarimón, J., Blesa, R., Lleó, A., for the Alzheimer's Disease Neuroimaging, I., 2014. Cerebrospinal fluid β-amyloid and phospho-tau biomarker interactions affecting brain structure in preclinical Alzheimer disease. Ann. Neurol. 76, 223–230. https://doi.org/10.1002/ana.24186

Franzmeier, N., Ren, J., Damm, A., Monté-Rubio, G., Boada, M., Ruiz, A., Ramirez, A., Jessen, F., Düzel, E., Rodríguez Gómez, O., Benzinger, T., Goate, A., Karch, C.M., Fagan, A.M., McDade, E., Buerger, K., Levin, J., Duering, M., Dichgans, M., Suárez-Calvet, M., Haass, C., Gordon, B.A., Lim, Y.Y., Masters, C.L., Janowitz, D., Catak, C., Wolfsgruber, S., Wagner, M., Milz, E., Moreno-Grau, S., Teipel, S., Grothe, M.J., Kilimann, I., Rossor, M., Fox, N., Laske, C., Chhatwal, J., Falkai, P., Perneczky, R., Lee, J.-H., Spottke, A., Boecker, H., Brosseron, F., Fliessbach, K., Heneka, M.T., Nestor, P., Peters, O., Fuentes, M., Menne, F., Priller, J., Spruth, E.J., Franke, C., Schneider, A., Westerteicher, C., Speck, O., Wiltfang, J., Bartels, C., Araque Caballero, M.Á., Metzger, C., Bittner, D., Salloway, S., Danek, A., Hassenstab, J., Yakushev, I., Schofield, P.R., Morris, J.C., Bateman, R.J., Ewers, M., 2019. The BDNFVal66Met SNP modulates the association between beta-amyloid and hippocampal disconnection in Alzheimer's disease. Mol. Psychiatry. https://doi.org/10.1038/s41380-019-0404-6

Friston, K., Ashburner, J., Kiebel, S., Nichols, T., Penny, W., 2007. Statistical Parametric Mapping. Elsevier. https://doi.org/10.1016/B978-0-12-372560-8.X5000-1

Ganda, O.P., Rossini, A.A., Like, A.A., 1976. Studies on streptozotocin diabetes. Diabetes 25, 595–603.

Gano, L.B., Patel, M., Rho, J.M., 2014. Ketogenic diets, mitochondria, and neurological diseases. J. Lipid Res. 55, 2211–2228. https://doi.org/10.1194/jlr.R048975

Gispert, J.D., Rami, L., Sánchez-Benavides, G., Falcon, C., Tucholka, A., Rojas, S., Molinuevo, J.L., 2015. Nonlinear cerebral atrophy patterns across the Alzheimer's disease continuum: impact of APOE4 genotype. Neurobiol. Aging 36, 2687–2701. https://doi.org/10.1016/j.neurobiolaging.2015.06.027

Griffanti, L., Douaud, G., Bijsterbosch, J., Evangelisti, S., Alfaro-Almagro, F., Glasser, M.F., Duff, E.P., Fitzgibbon, S., Westphal, R., Carone, D., Beckmann, C.F., Smith, S.M., 2017. Hand classification of fMRI ICA noise components. Neuroimage 154, 188–205. https://doi.org/10.1016/j.neuroimage.2016.12.036

Gudala, K., Bansal, D., Schifano, F., Bhansali, A., 2013. Diabetes mellitus and risk of dementia: A meta-analysis of prospective observational studies. J. Diabetes Investig. 4, 640–650. https://doi.org/10.1111/jdi.12087

Heo, J.-H., Lee, S.-R., Lee, S.-T., Lee, K.-M., Oh, J.-H., Jang, D.-P., Chang, K.-T., Cho, Z.-H., 2011. Spatial Distribution of Glucose Hypometabolism Induced by Intracerebroventricular Streptozotocin in Monkeys. J. Alzheimers Dis. 25, 517–523. https://doi.org/10.3233/JAD-2011-102079

Hölscher, C., 2019. Insulin Signaling Impairment in the Brain as a Risk Factor in Alzheimer's Disease. Front. Aging Neurosci. 11, 88. https://doi.org/10.3389/fnagi.2019.00088

Jack, C.R., Knopman, D.S., Jagust, W.J., Petersen, R.C., Weiner, M.W., Aisen, P.S., Shaw, L.M., Vemuri, P., Wiste, H.J., Weigand, S.D., Lesnick, T.G., Pankratz, V.S., Donohue, M.C., Trojanowski, J.Q., 2013. Tracking pathophysiological processes in Alzheimer's disease: an updated hypothetical model of dynamic biomarkers. Lancet Neurol. 12, 207–216. https://doi.org/10.1016/S1474-4422(12)70291-0

Jelescu, I.O., Budde, M.D., 2017. Design and Validation of Diffusion MRI Models of White Matter. Front. Phys. 5, 61. https://doi.org/10.3389/fphy.2017.00061

Jelescu, I.O., Shepherd, T.M., Novikov, D.S., Ding, Y.-S., Ades-Aron, B., Smith, J., Vahle, T., Babb, J.S., Friedman, K.P., de Leon, M.J., Golomb, J.B., Galvin, J.E., Fieremans, E., 2018. Spatial relationships between white matter degeneration, amyloid load and cortical volume in amnestic mild cognitive impairment. bioRxiv 441840. https://doi.org/10.1101/441840

Jelescu, I.O., Veraart, J., Fieremans, E., Novikov, D.S., 2016. Degeneracy in model parameter estimation for multi-compartmental diffusion in neuronal tissue. NMR Biomed 29, 33–47. https://doi.org/10.1002/nbm.3450

Jenkinson, M., Bannister, P., Brady, M., Smith, S., 2002. Improved Optimization for the Robust and Accurate Linear Registration and Motion Correction of Brain Images. NeuroImage 17, 825–841. https://doi.org/10.1006/nimg.2002.1132

Jensen, J.H., Helpern, J.A., Ramani, A., Lu, H., Kaczynski, K., 2005. Diffusional kurtosis imaging: The quantification of non-gaussian water diffusion by means of magnetic resonance imaging. Magn. Reson. Med. 53, 1432–1440. https://doi.org/10.1002/mrm.20508

Jespersen, S.N., Olesen, J.L., Hansen, B., Shemesh, N., 2018. Diffusion time dependence of microstructural parameters in fixed spinal cord. NeuroImage 182, 329–342. https://doi.org/10.1016/j.neuroimage.2017.08.039

Junod, A., Lambert, A.E., Stauffacher, W., Renold, A.E., 1969. Diabetogenic action of streptozotocin: relationship of dose to metabolic response. J Clin Invest 48, 2129–39. https://doi.org/10.1172/jci106180

Kametani, F., Hasegawa, M., 2018. Reconsideration of Amyloid Hypothesis and Tau Hypothesis in Alzheimer's Disease. Front. Neurosci. 12, 25. https://doi.org/10.3389/fnins.2018.00025

Kellner, E., Dhital, B., Kiselev, V.G., Reisert, M., 2016. Gibbs-ringing artifact removal based on local subvoxel-shifts: Gibbs-Ringing Artifact Removal. Magn. Reson. Med. 76, 1574–1581. https://doi.org/10.1002/mrm.26054

King, A., 2018. The search for better animal models of Alzheimer's disease. Nature 559, S13–S15. https://doi.org/10.1038/d41586-018-05722-9

Knezovic, A., Osmanovic-Barilar, J., Curlin, M., Hof, P.R., Simic, G., Riederer, P., Salkovic-Petrisic, M., 2015. Staging of cognitive deficits and neuropathological and ultrastructural changes in streptozotocin-induced rat model of Alzheimer's disease. J Neural Transm Vienna 122, 577–92. https://doi.org/10.1007/s00702-015-1394-4

Kraska, A., Santin, M.D., Dorieux, O., Joseph-Mathurin, N., Bourrin, E., Petit, F., Jan, C., Chaigneau, M., Hantraye, P., Lestage, P., Dhenain, M., 2012. In Vivo Cross-sectional Characterization of Cerebral Alterations Induced by Intracerebroventricular Administration of Streptozotocin. PLoS ONE 7, 1–9. https://doi.org/10.1371/journal.pone.0046196

Kuehn, B.M., 2020. In Alzheimer Research, Glucose Metabolism Moves to Center Stage. JAMA. https://doi.org/10.1001/jama.2019.20939

Kunz, N., da Silva, A.R., Jelescu, I.O., 2018. Intra- and extra-axonal axial diffusivities in the white matter: Which one is faster? NeuroImage 181, 314–322. https://doi.org/10.1016/j.neuroimage.2018.07.020

Lanz, B., Poitry-Yamate, C., Gruetter, R., 2014. Image-derived input function from the vena cava for 18F-FDG PET studies in rats and mice. J Nucl Med 55, 1380–8. https://doi.org/10.2967/jnumed.113.127381

Lester-Coll, N., Rivera, E.J., Soscia, S.J., Doiron, K., Wands, J.R., de la Monte, S.M., 2006. Intracerebral streptozotocin model of type 3 diabetes: relevance to sporadic Alzheimer's disease. J Alzheimers Dis 9, 13–33.

Montal, V., Vilaplana, E., Alcolea, D., Pegueroles, J., Pasternak, O., González-Ortiz, S., Clarimón, J., Carmona-Iragui, M., Illán-Gala, I., Morenas-Rodríguez, E., Ribosa-Nogué, R., Sala, I., Sánchez-Saudinós, M.-B., García-Sebastian, M., Villanúa, J., Izagirre, A., Estanga, A., Ecay-Torres, M., Iriondo, A., Clerigue, M., Tainta, M., Pozueta, A., González, A., Martínez-Heras, E., Llufriu, S., Blesa, R., Sanchez-Juan, P., Martínez-Lage, P., Lleó, A., Fortea, J., 2018. Cortical microstructural changes along the Alzheimer's disease continuum. Alzheimers Dement. J. Alzheimers Assoc. 14, 340–351. https://doi.org/10.1016/j.jalz.2017.09.013

Nitsch, R., Hoyer, S., 1991. Local action of the diabetogenic drug, streptozotocin, on glucose and energy metabolism in rat brain cortex. Neurosci. Lett. 128, 199–202. https://doi.org/10.1016/0304-3940(91)90260-Z

Novikov, D.S., Veraart, J., Jelescu, I.O., Fieremans, E., 2018. Rotationally-invariant mapping of scalar and orientational metrics of neuronal microstructure with diffusion MRI. NeuroImage 174, 518–538. https://doi.org/10.1016/j.neuroimage.2018.03.006

Pawela, C.P., Biswal, B.B., Hudetz, A.G., Schulte, M.L., Li, R., Jones, S.R., Cho, Y.R., Matloub, H.S., Hyde, J.S., 2009. A protocol for use of medetomidine anesthesia in rats for extended studies using task-induced BOLD contrast and resting-state functional connectivity. NeuroImage 46, 1137–1147. https://doi.org/10.1016/j.neuroimage.2009.03.004

Pegueroles, J., Vilaplana, E., Montal, V., Sampedro, F., Alcolea, D., Carmona-Iragui, M., Clarimon, J., Blesa, R., Lleó, A., Fortea, J., 2017. Longitudinal brain structural changes in preclinical Alzheimer's disease. Alzheimers Dement. 13, 499–509. https://doi.org/10.1016/j.jalz.2016.08.010

Plaschke, K., Kopitz, J., Siegelin, M., Schliebs, R., Salkovic-Petrisic, M., Riederer, P., Hoyer, S., 2010. Insulin-Resistant Brain State after Intracerebroventricular Streptozotocin Injection Exacerbates Alzheimer-like Changes in Tg2576 AβPP-Overexpressing Mice. J. Alzheimers Dis. 19, 691–704. https://doi.org/10.3233/JAD-2010-1270

Reynaud, O., da Silva, A.R., Gruetter, R., Jelescu, I.O., 2019. Multi-slice passband bSSFP for human and rodent fMRI at ultra-high field. J. Magn. Reson. 305, 31–40. https://doi.org/10.1016/j.jmr.2019.05.010

Shankar, G.M., Walsh, D.M., 2009. Alzheimer's disease: synaptic dysfunction and Aβ. Mol. Neurodegener. 4, 48. https://doi.org/10.1186/1750-1326-4-48

Shaw, L.M., Vanderstichele, H., Knapik-Czajka, M., Clark, C.M., Aisen, P.S., Petersen, R.C., Blennow, K., Soares, H., Simon, A., Lewczuk, P., Dean, R., Siemers, E., Potter, W., Lee, V.M.-Y., Trojanowski, J.Q., Alzheimer's Disease Neuroimaging Initiative, 2009. Cerebrospinal fluid biomarker signature in Alzheimer's disease neuroimaging initiative subjects. Ann. Neurol. 65, 403–413. https://doi.org/10.1002/ana.21610

Shoham, S., Bejar, C., Kovalev, E., Weinstock, M., 2003. Intracerebroventricular injection of streptozotocin causes neurotoxicity to myelin that contributes to spatial memory deficits in rats. Exp. Neurol. 184, 1043–1052. https://doi.org/10.1016/j.expneurol.2003.08.015

Sierra-Marcos, A., 2017. Regional Cerebral Blood Flow in Mild Cognitive Impairment and Alzheimer's Disease Measured with Arterial Spin Labeling Magnetic Resonance Imaging. Int. J. Alzheimers Dis. 2017, 5479597–5479597. https://doi.org/10.1155/2017/5479597

Smith, S.M., Jenkinson, M., Woolrich, M.W., Beckmann, C.F., Behrens, T.E.J., Johansen-Berg, H., Bannister, P.R., De Luca, M., Drobnjak, I., Flitney, D.E., Niazy, R.K., Saunders, J., Vickers, J., Zhang, Y., De Stefano, N., Brady, J.M., Matthews, P.M., 2004. Advances in functional and structural MR image analysis and implementation as FSL. NeuroImage 23, S208–S219. https://doi.org/10.1016/j.neuroimage.2004.07.051

Sperling, R.A., Aisen, P.S., Beckett, L.A., Bennett, D.A., Craft, S., Fagan, A.M., Iwatsubo, T., Jack, C.R., Kaye, J., Montine, T.J., Park, D.C., Reiman, E.M., Rowe, C.C., Siemers, E., Stern, Y., Yaffe, K., Carrillo, M.C., Thies, B., Morrison-Bogorad, M., Wagster, M.V., Phelps, C.H., 2011. Toward defining the preclinical stages of Alzheimer's disease: Recommendations from the National Institute on Aging-Alzheimer's Association workgroups on diagnostic guidelines for Alzheimer's disease. Alzheimers Dement. 7, 280–292. https://doi.org/10.1016/j.jalz.2011.03.003

van de Looij, Y., Kunz, N., Huppi, P., Gruetter, R., Sizonenko, S., 2011. Diffusion tensor echo planar imaging using surface coil transceiver with a semiadiabatic RF pulse sequence at 14.1T. Magn Reson Med 65, 732–7. https://doi.org/10.1002/mrm.22656

Veraart, J., Novikov, D.S., Christiaens, D., Ades-aron, B., Sijbers, J., Fieremans, E., 2016. Denoising of diffusion MRI using random matrix theory. NeuroImage 142, 394–406. https://doi.org/10.1016/j.neuroimage.2016.08.016

Veraart, J., Novikov, D.S., Fieremans, E., 2018. TE dependent Diffusion Imaging (TEdDI) distinguishes between compartmental T2 relaxation times. NeuroImage 182, 360–369. https://doi.org/10.1016/j.neuroimage.2017.09.030

Veraart, J., Sijbers, J., Sunaert, S., Leemans, A., Jeurissen, B., 2013. Weighted linear least squares estimation of diffusion MRI parameters: Strengths, limitations, and pitfalls. NeuroImage 81, 335–346. https://doi.org/10.1016/j.neuroimage.2013.05.028

Wang, L., Brier, M.R., Snyder, A.Z., Thomas, J.B., Fagan, A.M., Xiong, C., Benzinger, T.L., Holtzman, D.M., Morris, J.C., Ances, B.M., 2013. Cerebrospinal Fluid Aβ42, Phosphorylated Tau $_{181}$, and Resting-State Functional Connectivity. JAMA Neurol. https://doi.org/10.1001/jamaneurol.2013.3253

Weber, R., Ramos-Cabrer, P., Wiedermann, D., van Camp, N., Hoehn, M., 2006. A fully noninvasive and robust experimental protocol for longitudinal fMRI studies in the rat. Neuroimage 29, 1303–10. https://doi.org/10.1016/j.neuroimage.2005.08.028

Wu, L., Zhang, X., Zhao, L., 2018. Human ApoE Isoforms Differentially Modulate Brain Glucose and Ketone Body Metabolism: Implications for Alzheimer's Disease Risk Reduction and Early Intervention. J. Neurosci. 38, 6665–6681. https://doi.org/10.1523/JNEUROSCI.2262-17.2018

Yang, H., Shan, W., Zhu, F., Wu, J., Wang, Q., 2019. Ketone Bodies in Neurological Diseases: Focus on Neuroprotection and Underlying Mechanisms. Front. Neurol. 10. https://doi.org/10.3389/fneur.2019.00585

Zarow, C., Vinters, H.V., Ellis, W.G., Weiner, M.W., Mungas, D., White, L., Chui, H.C., 2005. Correlates of hippocampal neuron number in Alzheimer's disease and ischemic vascular dementia. Ann. Neurol. 57, 896–903. https://doi.org/10.1002/ana.20503

Zerbi, V., Grandjean, J., Rudin, M., Wenderoth, N., 2015. Mapping the mouse brain with rs-fMRI: An optimized pipeline for functional network identification. NeuroImage 123, 11–21. https://doi.org/10.1016/j.neuroimage.2015.07.090